Radio Astronomical Observing Lab Report

A7

Jacob Cardinal Tremblay, Pranav Limaye

April 26, 2022

S264

Contents

1 Introduction

This experiment consists of many important parts, which all contribute to the overall goal of helping introduce Master's students a scientific project involving radio astronomy. The first part is the technical theory behind how a telescope functions, and the concepts behind the types of observations which are performed in this experiment. This theory includes many important aspects of radio astronomical observation such as important mechanisms and fundamental equations which radio astronomers of all levels use today. Once at the telescope site, the operators guide the students around the telescope site, while explaining the important hardware components. After the required background knowledge, it is time to test the theory by applying it to real data. To do this, the data is first taken using a 25 meter Stockert radio telescope while making sure to apply the proper settings and techniques in order to produce good data. Such a telescope is an ideal introductory tool, as it has most of the same functionalities as state of the art telescopes, yet, since it is smaller and older, there is less demand to use the telescope and therefore it is less restricting in terms of applying for telescope time. Data is taken for a Milky Way calibration source, HI 21-cm line emission from a galaxy, and a bright pulsar. The data from this observation can then be taken and used for data reduction in order to arrive at scientific results which resemble what one would get while working for a radio astronomy focused research group.

2 Basics of Radio Astronomy

This introduction to the world of radio astronomy is our very own summary and interpretation of the topics mentioned in the 2022 lab manual by Jürgen Kerp, along with other sources which are cited. Please view the information in this report as a concise version of the material, focused around the specific tasks performed. For a

full understanding, please seek information from our cited sources.

Although radio astronomy has been around for a long time, the use of radio waves to understand the universe was not a priority at first. It wasn't until 1930, when Karl Jansky was studying distortions in Bell Laboratory's telecommunication that he discovered that radio sources at the center of the Milky Way galaxy. The synchrotron radiation he observed demonstrated that it was possible to study the universe at radio wavelengths. Although this study of the universe at radio wavelengths did not start until Grote Reber constructed his own telescope and explored the radio emission of the Milky Way Galaxy. The advancements in radar technology during World War II ultimately then aided the development of better radio telescopes and for radio astronomy to really take off as a research field.

2.1 The Interstellar Medium of the Milky Way Galaxy

The interstellar medium (ISM) in the Milky Way Galaxy is mainly composed of dust and gas, where dust is composed of massive agglomerations of Carbon and Silicate structures and gas is the complex composition of atoms and molecules primarily consisting of hydrogen. At longer wavelengths, dust structures emit as a Blackbody but can range in sizes from micrometer dust grains to heavy molecules which have large amounts of spinning atomic structures. This dust and gas can then become heated and ionized from the extra-galactic background due to its strong and high-energy radiation.

In the context of this course, only hydrogen will be studied due to its abundance. The neutral phase of atomic hydrogen will be investigated by HI 21-cm line measurements. To do this, an understanding of the basic technological concept of observation this line will be needed as well as the understanding of the local-standard-of-rest concept and calibration of HI observations. This Ionized hydrogen will be measured by pulsar dispersion measurements. The broad band pulse emitted by pulsars can range from

γ-rays to long radio waves. This means that a pulsar signal travelling through the ionized interstellar medium will have a dispersion of the signal because the electric component of the gas transfers high and low frequency radiation at different group velocities. This then leads to different arrival times for different wavelengths of the same pulsar pulse, which is what will be measured and quantified in this experiment.

2.2 Pulsars: dispersion of signals

A pulsar (shown in figure 1) is a rapidly spinning neutron star which is about the 15km in diameter and can theoretically have masses of $0.1M_{\odot}$ to $2.5M_{\odot}$ [6]. Such an object forms as a remnant from a massive star which has undergone supernova. The conservation in momentum from the large star spinning slowly will that translate this rotation to the small neutron star and therefore make it rotate extremely fast. This means that pulsars can have spin periods which range from seconds to milliseconds. This matter inside a neutron star is so extremely compact that the volume densities are similar to an atomic nucleus. Another important aspect of pulsars is that they have the strongest magnetic fields in the universe.

When the rotational axis is tilted against the magnetic axis, it is possible to observe an electromagnetic signal. Radiation will escape from the neutron star's surface along the magnetic axis. If this magnetic axis is aligned with the earth's line of sight, it is then possible to observe the pulsing signal. If this axis is not aligned correctly with the line of sight, the only detectable signal will be the blackbody radiation from the neutron star.

Because the pulsar spectrum at radio wavelengths approximately follows the relationship of $v^{-1.7}$, signals at higher frequencies will be fainter whereas signals at lower frequencies will be stronger. This means that in order to best study the effects behaviour of dispersion measure, low frequency and large bandwidths are needed. This is why instruments such as the Canadian Hydrogen Intensity Mapping Experiment

(CHIME) and the Low Frequency Array (LOFAR) are so important to such measurements as CHIME observes at a frequencies of 400-800 MHz [19] and LOFAR at frequencies of 150 MHz with a bandwidth of about 80 Mhz [17]. With other telescopes such as the Stockert telescope which will be used for this experiment, the observation can be made at 1.4 GHz, which is still a rather low frequency and the signals will be strong enough for this analysis. Being able to observe such a broadband signal can also be quite useful, as it allows the investigation of the signal creation close to the surface of the neutron star, however, it also allows for the analysis of the transfer of the pulsed frequency package through the ISM.

The time for a pulsar signal to travel a certain distance can be compared to the time that the same signal needs to travel in a vacuum. This gives a temporal delay represented by,

$$\Delta t = \int_0^d \frac{dl}{v_G} - \frac{d}{c}. \tag{1}$$

Where Δt is the temporal offset between the wave package which is transferred through the ISM and the time $\frac{d}{c}$ of a wave packet in a perfect vacuum. For the ISM,

$$t\,[s] \simeq 4.15 \cdot 10^3 \int_0^d n_e dl \cdot v^{-2}\,[\mathrm{MHz}]\,. \tag{2}$$

Where n_e gives the electron density and v is the observing frequency in MHz. Dispersion measure is then represented by,

$$DM = \int_0^d n_e dl \left[pc \cdot cm^{-3}\right], \tag{3}$$

which can be directly inferred from observations in radio wavelengths.

Because pulsars are so bright and their signals are well characterized and consistent, they are an ideal tool to study the DM of the ISM. By observing the time delay in the signal received at different frequencies, all that is needed is the appropriate volume density to then estimate the distance from the observer to the pulsar.

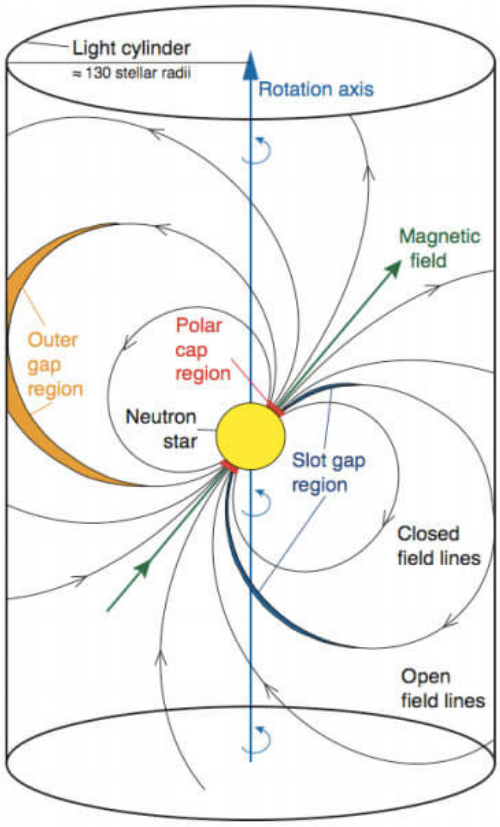

Figure 1: Basic components of a pulsar. Source: Cherenkov Telescope Array

2.3 The neutral atomic hydrogen line at 21-cm wavelength

Hydrogen is the most abundant element in the universe and although most is currently contained in stars, there still exists huge amounts of neutral hydrogen distributed along all the lines of sight in the Milky Way Galaxy. This makes neutral hydrogen an ideal tracer for the dynamics and mass distribution of the Milky Way.

Following the years when the HI-21cm line was first detected, it was mainly used to study the structure of the milky way and try to confirm its spiral shape. Neutral atomic hydrogen can also be interesting to study for other reasons than its abun-

dance. When optical light travels from distant stars, it will be strongly attenuated by intervening dust in a process known as extinction. Photons which have energies of a few eVs will not allow the disclosure of the large scale structure of the Milky Way however, the 21-cm line is perfect for such a task. This is due to the fact that the HI line is easily excited by the inelastic collision of atoms. Therefore, very small amounts of kinetic energy from atoms and molecules (10^{-6} eV) in interstellar space can excite neutral hydrogen. The lifetime of this excited state is also of the order of millions of years, which according to the energy-time uncertainty relation $\Delta E \times \Delta t \geq \frac{\hbar}{2}$ means that the natural width (ΔE) of the HI line is very narrow. HI photons can travel through the galaxy nearly unattenuated which leads leads it to being classified as "optically thin" radiation.

Because a photon has a spin of 1, the transition from neutral hydrogen $F = 1$ to $F = 0$ will emit a photon. $F = 1$ corresponds to when both the proton and the electron spin are oriented in the same direction whereas $F = 0$ corresponds to the anti-parallel orientation of both spins. The small energy difference between both states then emits a photon at the low frequency of 1420.405 MHz (21,1 cm wavelength). This transition gives an Einstein coefficient of $A_{10} = 2.85 \cdot 10^{-15}\text{s}^{-1}$, which in turn gives a lifetime of the excited state to be $t = \frac{1}{A_{10}} \simeq 3.5 \cdot 10^{14}\text{s} \simeq 11 \cdot 10^{6}$ years. This $F = 1$ is populated via collision however, collision also causes radiationless de-excitation in a high volume density environment such as a molecular cloud. The radiationless de-excitation by collision is the reason why for a long time it was not possible to produce the HI 21-cm line in a laboratory hence classifying the HI 21-cm line as belonging to a class of *forbidden* lines.

2.3.1 Line shape of the HI 21-cm radiation

Doppler motion can also be measured extremely precisely (to the $cm \cdot s^{-1}$) do to the extremely narrow ΔE line width. This line width is due to the fact that the $F = 1$ state has an extremely long lifetime Δt and the uncertainty relation: $\Delta E \times \Delta t \geq \frac{\hbar}{2}$.

Because of this and the fact that HI is so abundant, hydrogen is an ideal tracer for measuring interstellar gas as well as the entire Milky Way Galaxy. This is especially true since metalls are not of great importance and collisions with hydrogen atoms will couple their thermal motion to that of hydrogen.

Inelastic collisions between atoms and molecules in the interstellar medium couples different things together. The mass m of a particle and a kinetic energy E_{kin} will lead to a mass proportional velocity of $v \propto \frac{E_k}{m}$. The Maxwell distribution can describe the velocity distribution of such a group of particles. Using a radio telescope and spectrometer, the observation of a HI 21-cm line will show a line width much broader than the natural one usually located between 1 an $70 kms^{-1}$. The observed FWHM line width then gives the upper limit of the kinetic gas temperature T_{kin} by,

$$T_k \leq \frac{m_H \cdot \Delta v^2}{8 \cdot k_B \cdot \ln 2}. \tag{4}$$

The peak of such a Gaussian will be proportional to the brightness temperature T_B. We will expand upon the topic of the Rayleigh-Jeans law later in this report. However, we will anyways make the remark that if an isolated cloud is observed along the line of sight, the lower limit of the gas temperature can be estimated by the peak of the HI line whereas the upper limit can be determined by the FWHM of the Gaussian shaped profile.

2.3.2 The Local Standard of Rest

What appears to us as an unmoving rest frame is actually wrong. There is a lot of motion which we need to consider as we are located in a moving rest frame. This includes the motion of the earth around the Sun and the Sun's orbit around the Galactic center. In this moving rest frame, the local stellar environment of the Sun has been measured in velocity which introduces the local standard of rest frame. Thankfully, the telescope control system already takes all motion against the local standard rest frame into account, which can be identified by v_{LSR}.

The observation of a galaxy will give a different line shape than a Gaussian. In a galaxy, the rotation of the whole galaxy will smear out individual Gaussian line profiles and instead the countless individual clouds will be superimposed in the single line of sight. The different velocities of the gas clouds will then add up to the rotation curve of the galaxy, therefore the HI clouds will be able to describe the motion of the entire galaxy. As observers, the velocities which can be distinguished includes the systemic velocity which is the velocity of the galaxy as a whole and is equal to the red-shift. This means that the distance to this galaxy can be determined from the Hubble law. The second observed velocity can be measured from the FWHM of the galaxy's HI profile by using the the line width to measure for the mass of the galaxy. The stable rotation of a galaxy around its center means that the gravitation and centrifugal forces balance each other out. This leads to the relation that the larger the FWHM of the HI line, the larger the centrifugal forces needed, and therefore the larger the mass to balance them out.

2.3.3 Column density and baryonic gas mass

As previously mentioned, for optically thin gas clouds, the photons will travel through the universe without much absorption or scattering. This means that we can acquire the total number of hydrogen atoms along the line of sight directly from the brightness temperature and the line width. This is the column density defined by,

$$N_{\mathrm{HI}}\left[\mathrm{cm}^{-2}\right] = 1.8224 \times 10^{18} \int \frac{T_{\mathrm{B}}}{[\mathrm{K}]} d\left(\frac{v}{\left[\mathrm{km\ s}^{-1}\right]}\right) \tag{5}$$

Where $N_{textrmHI}$ represents the column density and T_{B} is the observed brightness temperature. One can the evaluate the HI mass of a galaxy in a similar manner.

The determination of the HI mass, M_H can be done by using the integration over the HI-line profile,

$$\frac{M_{\mathrm{HI}}}{M_{\odot}} \approx 2.36 \times 10^{5} \left(\frac{r}{\mathrm{Mpc}}\right)^{2} \int \frac{S_{\nu}}{\mathrm{Jy}} \left(\frac{dv}{\mathrm{km/s}}\right), \tag{6}$$

where r represents the distance to the source and S_v is the specific flux. However, the mass measured using this method does not represent the total mass of a galaxy, but rather only the HI mass. To get the total mass of the galaxy, one must also consider the baryonic mass as well as the dark matter component. The dark matter depends on scales such as the ones shown in figure 2. Therefore in order to estimate the total mass, we need to estimate the abundance of dark matter in the galaxy relative to the measured HI mass.

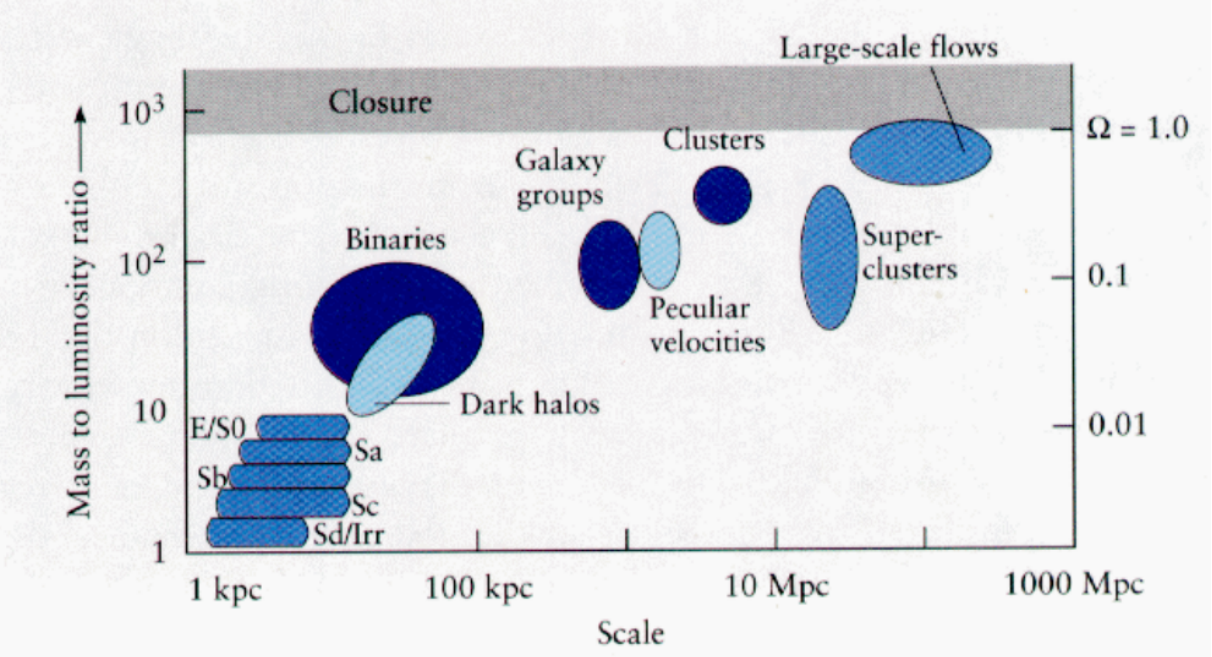

Figure 2: Celestial objects at different linear scales will have different proportions of baryonic and dark matter. Source: University of Oregon astronomy course, lecture 23.

3 Physical Background

3.1 Thermal radio emission

A radio telescope collects electromagnetic (EM) waves and focuses them on the feed which generates a certain equivalent current which is later processed by the back-end systems. The most commonly observed radio emission from the sky is thermal emission. Electromagnetic waves carry energy given by the Planck Energy ($E = h\nu$). Various thermal emission mechanisms contribute in producing this energy spectrum in the radio regime.
EM waves are generated when electrons get accelerated. Thermal emission occurs when such an acceleration of electrons takes place due to Thermal Brehmsstralung, Compton scattering or electron transition giving emission lines. If the electron acceleration takes place at relativistic velocities, it causes synchrotron emission. However, thermal emission can be characterized by the Black Body Spectrum and at the low radio frequencies, the brightness distribution is described by the Planck's law as

$$B(\nu)(T) = \frac{2h\nu^3}{c^2} \frac{1}{e^{\frac{h\nu}{kT}} - 1} \tag{7}$$

From this equation, we can see that $B(\nu)$ scales as ν^3. Hence for processes dominated by thermal emission mechanism, we expect the source flux increase cubically as a function of the observing frequency but at the same time, higher frequency means high energy and we receive much less photons to produce the desired SNR.

3.2 Synchrotron radio emission

In the last section it was discussed how the brightness increases as a function of the frequency. This is a result of thermal emission processes. However, it is seen that the most dominant radio emission in the Universe occurs at very low radio frequencies

in the range of a few hundred MHz. The interstellar medium is filled with magnetic fields which accelerate the stellar free electrons to relativistic velocities producing synchrotron radio emission. This emission follows a power-law brightness distribution with a negative spectral index, i.e, $B(\nu) \propto \nu^{-\alpha}$ where for most astrophysical sources, $\alpha = 0.75$ [21].
Pulsars are the most unique objects producing the strongest magnetic fields $\sim 10^{12}G$ [21]. Pulsar radio emission is a synchrotron radiation originating from the dipolar magnetic fields and hence, Pulsars are very bright at low radio frequencies.

3.3 Intensity, brightness and power

Intensity: This term is often confusing. In Radio Astronomy jargon, it is called the 'Specific Intensity (I_ν)' defining the energy emitted by a source per unit frequency. Therefore, it is important to note here that specific intensity is a distance independent quantity and only depends on the intrinsic characteristics of the source.
Brightness: Brightness is the integral of the received source intensity I_ν over all the frequency coverage. The detector area $d\sigma$, the inclination of source with respect to the telescope θ, integration time dt and the antenna solid angle $d\Omega$ also contribute in determining the observed brightness of the source which is given by,

$$dE = I_\nu cos\theta d\sigma d\Omega dt d\nu \tag{8}$$

Power: The quantity Power (dP) is the energy received from the source per unit time which is the main quantity of interest for us also called as the 'received flux'. It is given by,

$$dP = \frac{dE}{dt} = I_\nu cos\theta d\sigma d\Omega d\nu \quad Watts(m^2 SrHz) \tag{9}$$

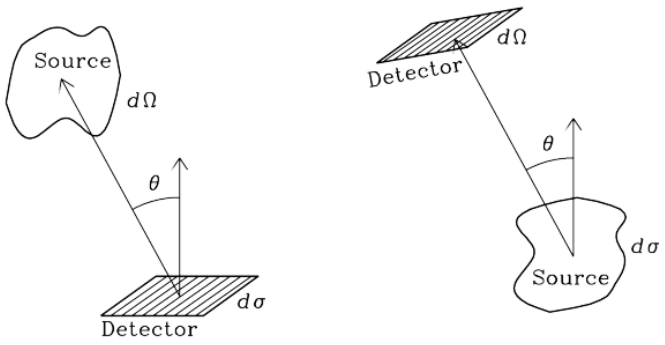

Figure 3: Telescope and source orientation representation depicting the important telescope parameters which affect the received flux (source: Essential Radio Astronomy)

4 Radio Telescopes

4.1 System temperature

Although a "perfect" radio telescope would only receive radiation from the source, in practice, radio telescopes receive radiation from their entire environment. The main lobe is the antenna's maximum sensitivity and receives approximately 70% of all incoming radiation. The rest of the radiation is received by the near- and far-side lobes which can also be called stray lobes. The main lobe can be comparable to the main maximum of an airy disk, whereas the stray lobes are equivalent to the ring shaped diffraction pattern that encircles the maximum of the Airy disk. If there are no obstacles, the incident photons will be focused at the center of the Airy disk and the diffraction rings will be comparatively small. However, for radio telescopes a much larder amount of the incident photons are collected by the side-lobes due to aperture "blocking".

There are typically 5 sources of radiation which will be contained in the data which

make it harder to measure the radiation coming uniquely from the source, T_{source}. The cosmic microwave background noise, T_{CMB}, the diffuse synchrotron radiation of the Milky Way, $T_{syn}(v = 1420MHz) \simeq 0.1$ K with $v^{-2.7}$, the Earth's atmosphere, T_{atm}, the spill-over T_{spill}, and the thermal noise of the receiver $T_{receiver}$ all contribute to the noise and can be added up linearly so that the brightness temperature received is described by:

$$T_{sys} = T_{source} + T_{CMB} + T_{syn} + T_{atm} + T_{spill} + T_{receiver}. \tag{10}$$

The source will most always be faint compared to the system temperature, making it important that the amplifier (whose thermal noise dominates the receiver chain) be cooled in order to increase the signal-to-noise ratio. An actively cooled system would be at a temperature of about 18 K for 21-cm wavelength observations.

4.1.1 The atmospheric window

The Earth's atmosphere is a complex turbulent medium of gas and ionized particles. This fact protects the life on the planet from high energy cosmic radiation but due to the blockage to UV and X-rays, it becomes very difficult to do astronomy and we have to send scientific probes outside the atmosphere. However, this is not the case for Radio waves. There is a wide radio frequency range called the 'radio window' which can pass through the atmosphere with minimum attenuation.
The upper band of this window, i.e, the high frequency GHz radio waves are absorbed by the atmospheric gases suffering from high signal attenuation. On the other hand, Low frequency signals get reflected off from the atmosphere. The qualitative measure of reception of these signals is given by the transparency of the atmosphere to the waves. Water vapor (H_2O) and CO molecules are the major greenhouse gases that hinder the atmospheric transparency to radio waves. Therefore at a Radio Observatory, one also finds a Water Vapor Radiometer (WPR) to keep track of the variations in these atmospheric layers allowing the observer to choose the observing parameters accordingly to get a good SNR for the observation.

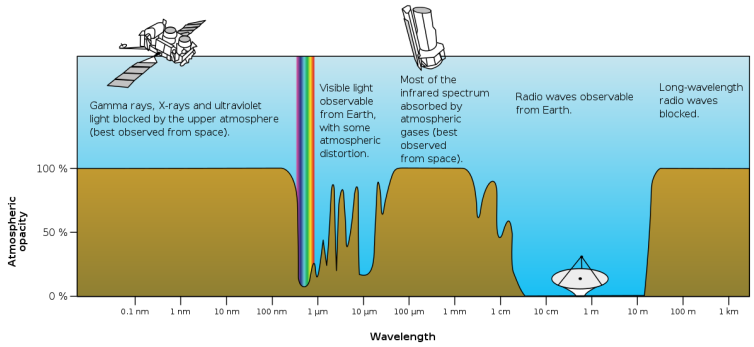

Figure 4: The atmospheric opacity for the entire EM spectrum (source:wikipedia)

4.1.2 Radiometer equation

The radiometer equation is an important equation as it gives a measure for the quality of the observation. It is represented as,

$$\Delta T = \frac{T_{sys}}{\sqrt{\Delta\nu \cdot \Delta t}} \tag{11}$$

Where Δv is the bandwidth, Δt is the length of the observation and ΔT is the uncertainty in the determination of the source brightness temperature. From the product of the bandwidth and duration of observation, a measure for the energy received is determined: $\Delta E = \propto (h)\Delta v \cdot \Delta t$. This relation means that if the integration time is increased, then the number of received photons will be higher. This is also true if the bandwidth is increased. The observation of a faint source will require a longer integration time so that more photons from the object may be captured.

4.2 Radiometer

The receiving unit of a radio telescope that captures the space EM radio waves and does the further signal processing is collectively called a radiometer. To simplify things, a radiometer can be simplified into different sections as follows:

Receiving Dipole: This is the main part of the radiometer which acts as a coupling device between the sky radio waves and the receiver unit. The radio waves focused onto this feed are converted into electric current and to ensure minimum signal loss, the position of this dipole is usually proportional to $\lambda/4$.

Low Noise Amplifier(LNA): Radio waves coming from astronomical sources are very weak, of the order of a $\sim 10^{-26} Watts m^{-2} Hz^{-1}$. Therefore, before transferring the signal through cables, an amplifier block is placed after the dipole which amplifies the weak radio signal. LNA is not a single amplifier but is a multistage amplifier system having a cascade of Gaussian with the gain G1 of the first amplifier deciding the noise of the receiver system. Therefore, the first amplifying stage should always have the highest Gain factor to avoid any significant signal attenuation.

Filter: A band-pass filter allows signals of only a certain frequency bandwidth to pass through and blocks the other signals. This block is useful in taking spectroscopic observations, especially for galaxy spectral line observations which have a fixed frequency range of emission.

Square-Law Detector: The RF signal is of oscillating nature and we cannot simply add this signal as the effective signal strength will become zero due to the dual polarity cycles of the signal. Instead, the negative signal cycles are squared mostly using a diode circuitry and then integrated to get the effective power of the signal.

Integrator & Recorder: The squared signal from the diode detector is integrated into the integrator and then read-out on a recorder or a disk.

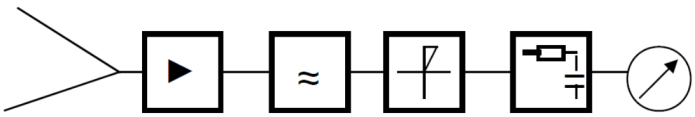

Figure 5: Different components of a radiometer (Feed $->$ Amplifier $->$ Band-pass $->$ Square-Law Detector $->$ Integrator $->$ Recorder); source: lab$_s cript$

4.3 Radio telescopes construction

Unlike other telescopes, radio telescopes can be constructed in two different configurations. Radio dish telescopes that converge the incoming em waves just like optical telescopes and dipole arrays which make use of the concept of phased arraying and interferometry to either study spatially high or low resolved sources in the sky. In the scope of this experiment, radio dish telescopes are of main concern. Larger the diameter of the dish, higher is the angular resolution since larger is the available collecting area. The angular resolution of a radio telescope is given similar to that of optical telescopes,

$$\theta = 1.22\frac{\lambda}{D}arcmin \tag{12}$$

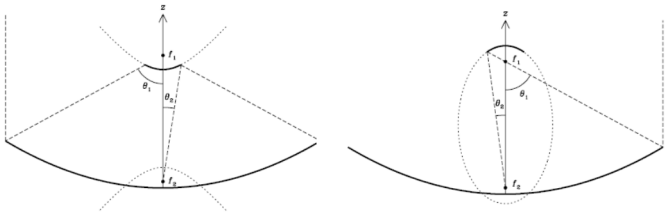

Figure 4.6: Left: optical layout of a Cassegrain telescope. **Right:** Optical design of a Gregory telescope. Image from the textbook "Essentials in radio astronomy, Chapter 3.

Figure 6: Radio Telescope Construction, (source: Essential Radio Astronomy). */

Based on the feed optics, dish radio telescopes can be classified into Cassegrain or Gregorian Construction. (refer 6).

The main motivation of using a Cassegrain feed is the small size and easy implementation at the feed-point. However, the Gaussian feed has an advantage that it has two focal points allowing the telescope to accommodate multiple frequency coverage feeds at these focal points.

4.3.1 Aperture blocking

The prime-focus of radio telescopes is supported by metallic arms. This structure blocks the in-falling radio waves falling on the dish. As a result of this, the sensitivity of the telescope decreases due to decrease in photon number and the angular resolution den degrades due to the diffraction of radio waves from this aperture blocking. This effect is much severe for making high frequency observations but can be tolerated for low frequency observations.
Refer 7 to see the power distribution of the radio waves at the focus due to the blocking aperture.

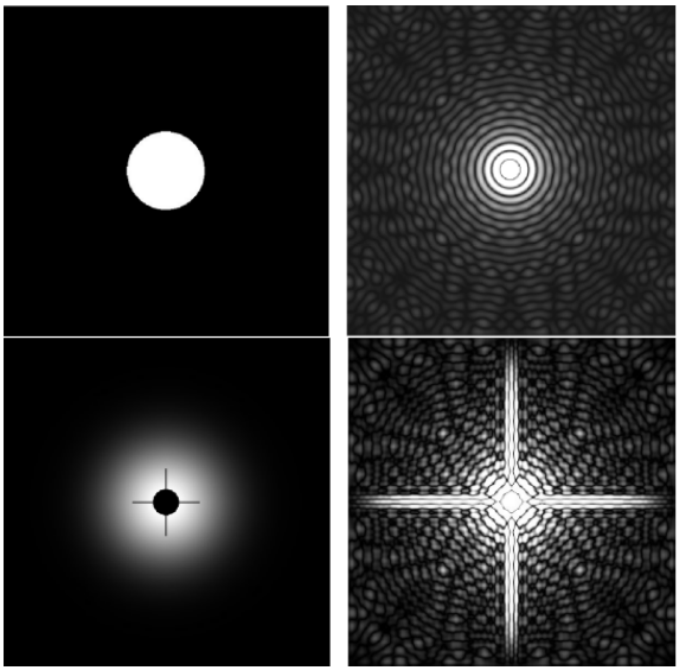

Figure 4.7: **Top left:** Ideal unblocked aperture with maximum transmission out to the rims of the telescope. **Top right:** Power distribution of the unblocked aperture. This is the well known Airy disk pattern realized in practice by a refracting telescope. **Bottom left:** Blocked aperture of a radio telescope. Because one aims to minimize the system temperature (see Sect. 4.1) one needs to minimize the *spill over* of the receiver. This is realized by a Gaussian taper here. **Bottom right:** Power distribution of that blocked aperture. The angular resolution is severely degraded (reduced) by the secondary mirror. The larger the secondary, the worse the angular resolution. The support legs cause the cross-like structure.

Figure 7: Antenna Aperture Blocking, (source: lab script)

4.4 Antenna diagram

Antenna Diagram is the most fundamental property used to study the response of the antenna to the frequency of the radio signals being collected by the telescope. It is used to study the antenna beam response. The antenna diagram is usually represented in the form of 'polar plots' where the scale 0dB corresponds to the maximum antenna sensitivity. (Refer 8) The above antenna diagram represents a

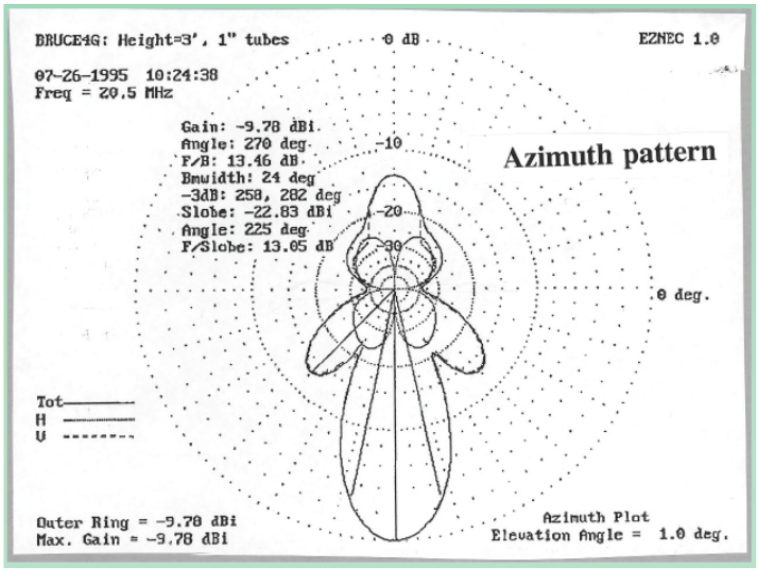

Figure 8: Polar Plot of a typical antenna beam response, (source: lab script)

dipolar field with two main lobes. The negative lobe is added to the positive main lobe using a reflector placed at an appropriate distance from the feed. Dipoles are in principal omni-directional receptors but in practice, the radio beam also consists of side-lobes which are susceptible to RFI and other terrestrial noise and are the major noise contributors in the main beam using which we intend to carry out the observations. Innovative methods like 'Adaptive Beamforming' are now been used to utilise these side-lobes such that their minima is pointed towards the noise sources using electronic beam-steering thus, giving a higher quality radio astronomical signal.

4.4.1 Surface accuracy

Surface accuracy gives the deviations in the reflecting material of the telescope thus causing the converging beams to defocus. This is a wavelength dependent quantity and hence, has no significant effect for low observing frequencies. However, surface accuracy is a major concern for high frequency observations as it will degrade the observing sensitivity if not corrected. Dish telescopes have actuators placed under each tile of the dish which constantly maintain the surface accuracy of the dish to a highly precised value.
If σ is the standard deviation from the ideal surface and λ is the wavelength, the surface smoothness η is given as,

$$\eta = e^{-(\frac{4\pi\sigma}{\lambda})^2} \tag{13}$$

4.5 Antenna temperature and brightness temperature

From the Rayleigh-Jeans Approximation we know that the flux received at the feed is proportional to the physical temperature of the emitting radio source. This value is called the Brightness Temperature 'T_B'. The brightness temperature is a value intrinsic to the source. The telescope measures the temperature value within the telescope beam considering the beam response which is termed the Antenna Temperature 'T_A'. For most observations, a small fraction of the beam is illuminated and the rest of the beam gets filled with unnecessary background photons. Hence, antenna temperature is a telescope dependent quantity and is different for different observing sites. However, a simple relation can be established between these two temperatures by,

$$\frac{T_A}{T_B} = \frac{\Omega_{source}}{\Omega_{Main_Beam}} \tag{14}$$

Due to the practicality of a telescope design, a radio telescope not only receives radiation from the main beam (Ω_{Main_Beam}) but also from the antenna sidelobes thus,

defining the main beam efficiency by the factor,

$$\eta = \frac{\Omega_{Main_Beam}}{\Omega_A} \tag{15}$$

where,
$\Omega_A -> \Omega_{Main_Beam} + \Omega_{stray}$

Using the information provided by the physics of our telescope, the aperture efficiency, and the Rayleigh-Jeans approximation we can get the conversion from Kelving to Jansky given the parameters for the 25-m Stockert telescope:

$$\frac{T\,[\mathrm{K}]}{S_{\mathrm{source}}\,[\mathrm{Jy}]} = \frac{A_{\mathrm{eff}}}{2k_{\mathrm{B}}} = \frac{\pi \cdot (12.5\mathrm{m} \cdot 0.7)^2}{2 \cdot 1.38 \times 10^{-23}\mathrm{JK}^{-1}} = 0.09 \tag{16}$$

4.6 Calibration of an HI observation and system temperature

The calibration of the telescope is an extremely important step in the process of HI observations. During this process, not only is the telescope calibrated, but the system temperature is measured by observing a standard position (S7, S8 or B8) from [1]. These sources are located in the plane of the milky way, which means the velocity profiles are broad. Basic properties such as peak brightness for these regions are listed in [1]. These need to be accounted for as the baseline of the observation. Once this baseline is removed, the peak brightness temperature and line integral can be evaluated. When performing the observation, the integration time should be long enough to minimize statistical uncertainties to less than 5%. The baseline is then subtracted after which the peak and integral across HI line can be calculated. These results should be compared with those in [1] and the ratio of both values will be the calibration factor α, which can then be used to calculate $T_B = \alpha \times T_A$.

4.7 Observing a pulsar

Pulsar observations are quite special astronomical observation therefore it is important to expand upon the topic.

Even though the radio emission is governed by coherent emission mechanism, the single radio pulses from pulsars are very weak to detect individually and are highly attenuated as they travel through the interstellar medium as a function of frequency. Therefore, detection of pulsars needed a new kind of approach in Radio Astronomy very different than traditional observing methods for observing galaxies and other bright sources.

Observing pulsars requires a high amount of instrument sensitivity and timing efficiency. Pulsars show great amount of periodicity which is also very stable over a long range. Radio Astronomers take advantage of this periodicity to detect pulsars in the radio sky and on stacking different pulses at intervals of the pulsar period, we get a pulse profile. However, the knowledge of period of a pulsar is not sufficient for its observation. The space between us and the pulsar is not a vacuum, but is filled up with all sorts of Interstellar Medium (ISM) matter like gas clouds, dust, plasma, etc. The radio beams coming from the pulsar are highly affected as they pass through the ISM and the factor by which a radio beam from a pulsar coming from a specific line of sight interstellar material is given by the **Dispersion Measure**. (see section 2.2 for more details)

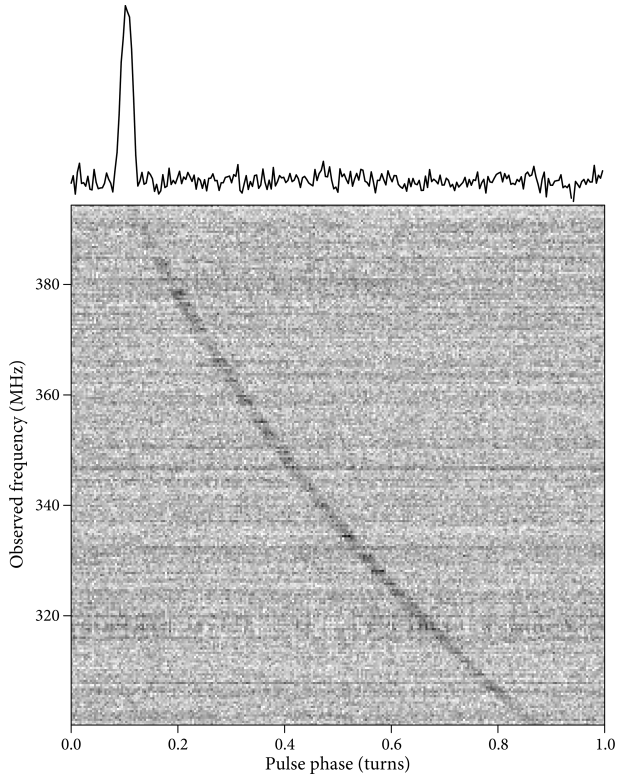

Figure 9: Delay in Time of Arrival of different frequency signals as a function of the pulse phase source: www.cv.nrao.edu)

5 Observations

5.1 Stockert Telescope

Before conducting the first steps of the experiment, it was important to take a tour of the instrumentation of the Stockert telescope and gain a general understanding of the instrument and how it operates. From the *Astropeiler Stockert eV* website [**?**], we know that this telescope has a primary parabolic dish of 25 meters in diameter, and is located in nearby Bad Münstereifel-Eschweiler.

The telescope is built on top of, and mounted on an octagonal structure built from concrete inside which is located the control room as well as other rooms which were not used in this experiment. Starting in the control room, most of the computers used to process the signal and convert it to useful information are located here. This is also where the controls are located, so the operator may tell the telescope where to look in the sky and and set the observation parameters to be appropriate for the type of observation which is being made.

The Stockert Telescope is equipped with a modern tracking system, therefore making it easy to follow an object in the sky as the earth rotates. This means that no action is needed by the operator (with respect to source tracking) while the telescope is observing. A particularly unique aspect of this telescope is that they have preserved a large amount of the original instrumentation, meaning that the old devices are still present and working with the telescope, however, a modern system has also been installed so that everything can be controlled by computers. This is quite special, as it allows for the ease of use of modern computer systems, while giving a unique "vintage" style to the instrumentation. Moving from the control room and further up to the radio dish, one can first spot the large amount of gears which are important to the Azimuth directions of the telescope mount, whereas the elevation part of the mount are located somewhat higher up. This leads us to conclude that the telescope

is using an elevation-azimuth mount, which is fully steerable, and according to [20], can cover -2° to 90° in elevation.

Moving even further up in the telescope, we arrive at the dish. This dish is made of from an AL-MG-Si F32 perforated aluminum sheet, which has hole sizes of 8×8 mm. Although the mirror has a parabolic shape, the deviation from this shape in in average $\sigma = 1.7$ mm. These deviations are quite small, therefore they do not affect the error in the measurement in any significant manner, and the mirror can be approximated as being parabolic. The telescope has capability to observe at frequencies of 1.4 GHz, 1.6 GHz, and 4 GHz and uses a primary focus system. This means that there is no secondary mirror, and that the receiver is mounted directly at the focal point of the dish. There are both downsides and upsides to having the receiver mounted in this way. These can include having a larger field of view, however spillover will be larger when compared to using a secondary dish.

On the receiver horn was a circular waveguide and two dual-polarization "cloverleaf" antennas [12]. If we follow the signal as it is input into the receiver, we first run into the low noise amplifier (LNA), and the local oscillator (LO), who down-converts the signal in a range of 100-200 MHz, which gives a bandwidth of 100 MHz. A band-pass also filters the frequency before and after the LO. Between the receiver and the control room, there are computers which access the signal, however the details were described as not being important to this experiment by the telescope operator. The signal is then transmitted to the control room using 10 Gb/s cables which feed into a converter which converts the analog signal to a digital signal. Then, by using an fast Fourier transform (FFT) spectrometer, the signal is converted to an intensity spectrum. This spectrometer can be set up in two separate modes. These modes are either used for galactic HI observation where the spectrum is integrated over a time of 1 second, or for pulsar observations, where the time resolution is extremely high. Because astronomical data (especially pulsar observations) deal with extremely precise measurements in time, it is important that the instrumentation is synced using the Rb atomic clock located in the control room.

5.2 Data reduction of the HI 21-cm line observations

Before completing the baseline correction and calibration for the calibration observation, it is important to discuss the Rayleigh-Jeans approximation of Planck's law in further detail. This approximation is made under the assumption that we are using low frequencies (which applies to radio wavelengths in the regime of MHz to THz), and states that emitted radiance is directly proportional to the black body temperature [23]. This approximation can be represented by,

$$B_\lambda(T) = \frac{2ck_BT}{\lambda^4}. \tag{17}$$

Where B is the spectral radiance, is the wavelength, c is the speed of light, k_b is the Boltzmann constant, and T is the Temperature.

This is relevant to our observation, because we are observing at the radio wavelength and therefore where the frequency is low enough for this approximation to apply. The energy of light normally transferred from an electromagnetic wave can be measured using $E = h\nu$. For radio waves, this would mean that the measured energy would be in the range of $4 \times 10^{-9}\text{eV} \leq h\nu \leq 4 \times 10^{-4}\text{eV}$. However, photon energies from the average kinetic gas in the Milky Way are measured to be much smaller ($\simeq 0.08$ eV), therefore we must use the approximation for $h\nu \ll k_BT$, which can also be represented in the form,

$$B_\lambda(T) = \frac{2\nu^2k_BT}{c^2}. \tag{18}$$

for frequency. For a black body, this equation is quite important, as there is a direct connection between the observed brightness of the source and the physical temperature. This therefore can be used to represent the measured intensity of a blackbody, since it's intensity along with its temperature at a given frequency would give the brightness temperature.

5.2.1 Baseline Correction and Calibration

The first step in taking HI data is always the calibration of the telescope by observing a calibration source of known flux and shape. This is done in order to calculate a calibration factor α which will allow us to convert the measured antenna temperature T_A to the true brightness temperature T_B of our source. For this project, the chosen source was S7 which is a very bright object ($T_B = 96.3 \pm 2.89$ K) which has consistent properties (shape and flux) for 21-cm line observations, where the brightness temperature value comes from figure 4 in [1], where the HPBW of the Stockert telescope corresponds to about 30 arcminutes and the uncertainty is given to be about 3%. Since the entire source must be inside the beam in order for it to be used as a calibrator, this source is only useful for any telescope beam smaller than about 1 degree. This applies to the Stockert Telescope (which has a HPBW of about 0.5°) therefore for this and all the above mentioned reasons, S7 is a good calibration source for this project.

Physically, this source is a bright section of the Milky Way, we can see in figure 10 that there are 3 peaks at different velocities. These peaks are caused because the line of sight intersects with 3 different spiral arms at 3 different distances therefore the signal peaks are coming from 3 different spiral arms of the Milky Way. This calibration source was observed using an integration time of 30 seconds. An important aspect to note is that during the observation period, there was a malfunction with the telescope system, and the computer which controlled the telescope position was not properly communicating with the signal processing computer. This meant that the system controlling the VLSR correction was not working properly, and therefore no VLSR correction will be applied to the data. This means that the measurement in the Doppler shift position will be shifted, and therefore the velocity position of the data will be inaccurate by a certain factor.

Once the data was taken (raw spectrum shown in figure 10), one can notice that the noise level of the spectrum are higher than $10K$, and seem to increase with channel

number. This is because the radio continuum emission is not being removed. In order to take this into account, one must subtract the baseline from the data. This baseline is determined by fitting a fifth order polynomial ($ax^5+bx^4+cx^3+dx^2+ex+f$) to the data points relatively close to the source but which were not part of the HI 21-cm line emission of the source. To create the fit, the `numpy.polyfit` [16] Python software was used, producing the baseline fit displayed by the red line in figure 11.The baseline was then subtracted from the original measurement, which gave the spectrum shown in figure 12. In order to properly show all the information in the plot, the x-axis was converted to a frequency axis and a velocity axis. This was done by using the frequency information given in the raw data, and converting it to the velocity using the Doppler formula (Eq. 19):

$$v = \left(1 - \frac{\nu}{\nu_0}\right) \cdot c. \tag{19}$$

Where for 21-cm line HI observations $\nu_0 = 1420.405$ MHz and $c = 299,792.458\,\mathrm{km\ s^{-1}}$. After removing the baseline, it is also important to remember that the spectrum has not yet been calibrated to the specifics of the telescope. To do this, a calibration factor must be calculated. From [1], we know that the peak of the brightness temperature at the S7 location is of 96.3 K. Therefore, we must adjust our measured values so the peak of the calibrated spectrum is also at 96.3 K. This is done by using the calibration factor given by equation,

$$\alpha = \frac{T_B}{T_A}, \tag{20}$$

Where the uncertainty is given by Gaussian error propagation,

$$\Delta\alpha = \left|\frac{T_B}{T_A^2}\Delta T_A\right|, \tag{21}$$

and the uncertainty in the antenna temperature after removing the baseline is calculated using the root mean square (RMS),

$$\Delta T_A = \mathrm{RMS}\,(T_A) = \sqrt{\frac{\Sigma_{\mathrm{baseline}} T_A^2}{N}}. \tag{22}$$

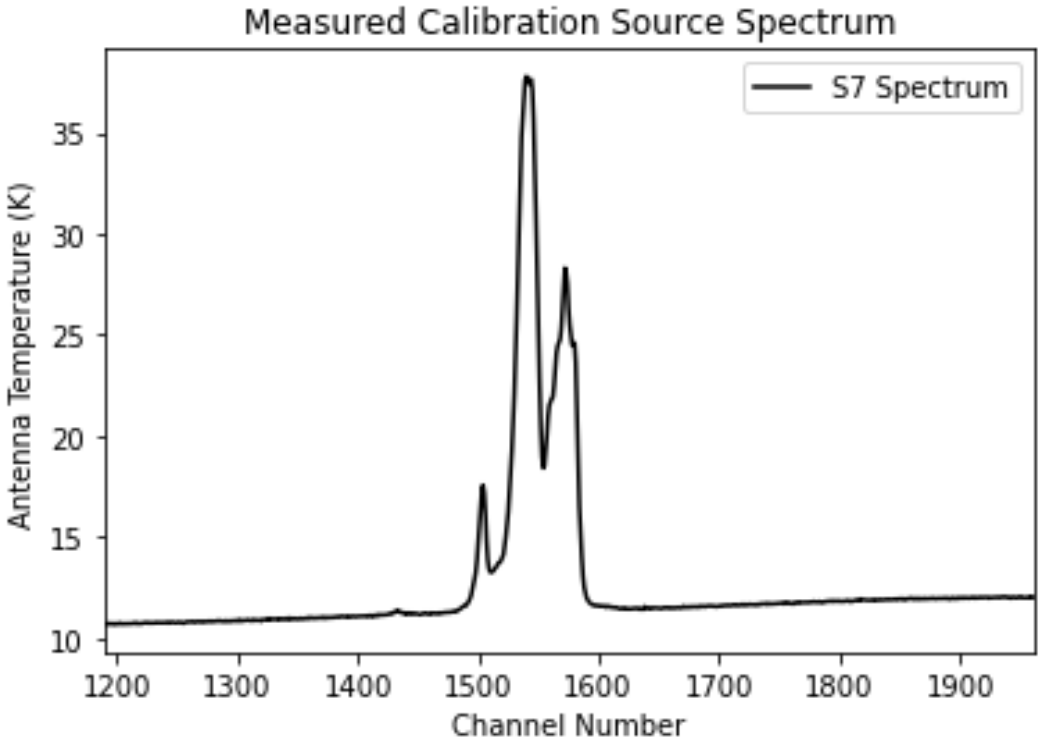

Figure 10: Spectrum of S7 calibration source.

Which yields an uncertainty in antenna temperature of $\Delta T_A = 4.51$ K. Using the `numpy.max()` function from the Numpy Python library [16] we then determined the maximum measured value of our HI profile to be an antenna temperature of $T_{A,max} = 26.4 \pm 4.51$ K, where the uncertainty is calculated from Eq.22. Using the previously mentioned S7 brightness temperature, along with the determined antenna temperature, we can now use Eq. 20 and Eq. 21 to calculate the calibration factor to be:

$$\alpha = 3.64 \pm 0.621. \tag{23}$$

This calibration factor is quite important as it now allows us to convert the baseline-subtracted antenna temperature to the actual brightness temperature spectrum shown in figure 13.

We can then calculate the system noise at T_B scale. To do this, we evaluate the ΔT_B in the same manner as was previously done for ΔT_A, using equation 22 but replacing ΔT_A by ΔT_B. This gives us a result of $\Delta T_B = 16.4$ K. We can then use the radiometer equation, Eq.11, to determine the system temperature. Using a spectral resolution of $\nu = 6.10 \times 10^{-3}$ MHz and an integration time of $\Delta t = 29.70$ s, we get a system temperature of:

$$T_{\text{sys}} = \Delta T_B \cdot \sqrt{\Delta\nu \cdot \Delta t} = 6994.61\text{K}. \tag{24}$$

Where no uncertainties are given on the values of frequency or time, therefore we cannot compute an uncertainty for the system temperature. Ideally, we would know the error in the systematics from the telescope, which could give an uncertainty in the recorded time of observation and the recorded frequency. The uncertainty in the atomic clock would be negligible however, as it is most likely tens of orders of magnitude below zero [13]. This leaves the possible uncertainty to other instrumentation which are a part of the telescope, however, it would be scientifically irresponsible to guess at the uncertainty, therefore giving us the motivation to leave the value of the system temperature without an uncertainty. This does however come with the additional warning that if one is to trust this value, they should first determine the uncertainty from the instrumentation that gives the values for time and frequency at the telescope site.

The value obtained for the system temperature is extremely high compared to usual values and is almost certainly non physical. The reason for this high value is most likely due to the fact that the uncertainty in the brightness temperature calculated, is itself many orders of magnitude larger than one would expect. For example, if we applied the same calculations using a brightness temperature of 3 orders of magnitude lower, we would obtain a reasonable result. However, since the high value in the uncertainty of the brightness temperature comes directly from our data, we must accept this result with the hopes of further proving or disproving this value in future observations.

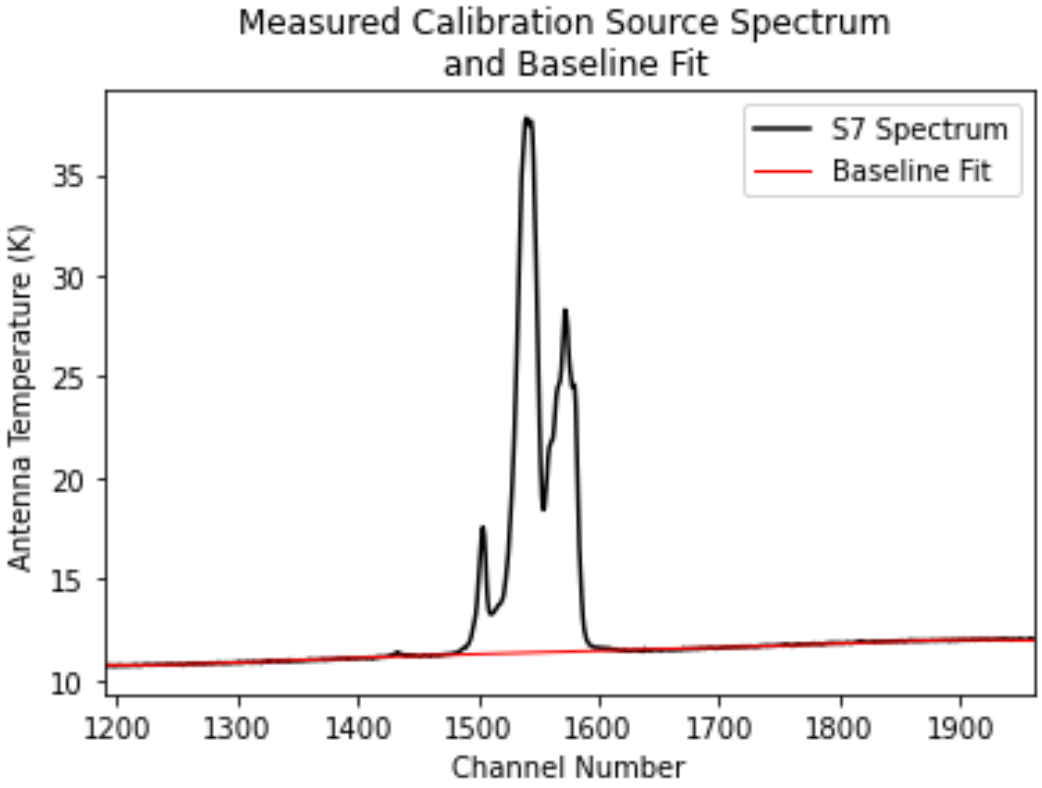

Figure 11: Spectrum of S7 calibration source with the appropriate baseline fit.

5.2.2 Observation of galaxy NGC 1073

The first galaxy chosen for observation was NGC 7714 which is a galaxy located in a pair of galaxies, at coordinate of right ascension: 23:36:14.126 and declination: +02:09:18.197 [18], radial velocity of 2790 km/s, and a redshift of z = 0.00935 [3]. A test observation of 5 minutes was done on this galaxy in order to determine if it was visible, as the lab teaching assistant noted that it had previously not been visible with the Stockert Telescope. After this observation, one can see from figure 14, that there is mostly just noise in the data, and we do not see the expected "double-horned" spectrum at the expected radial velocity. This means that the signal is most likely too faint to be detectable with the Stockert Telescope at this wavelength.

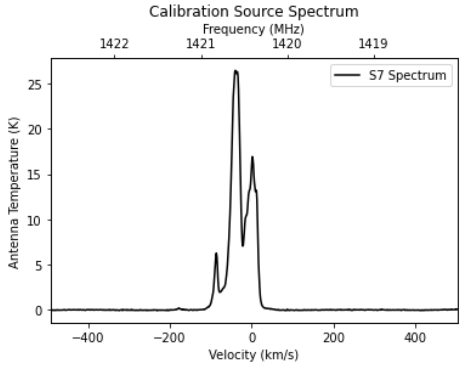

Figure 12: Spectrum of S7 calibration source with baseline subtracted.

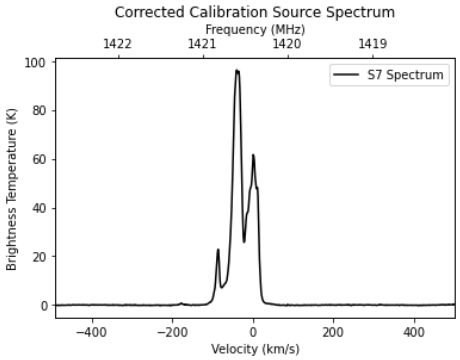

Figure 13: Calibrated spectrum of S7 with baseline subtracted.

Because NGC 7714 was not detected, a different galaxy was chosen for observation. Galaxy NGC 1073 (dislayed in figure 15 in optical wavelengths), which has a morphological type of SBc(sr) [2] was the next candidate for the galaxy observation. This galaxy has the coordinated of right ascension: 02:43:40.598 and declination: +01:22:33.13 [7], radial velocity of 1207.9 km/s, a redshift of z = 0.004037 [5] and is at a distance of 12.3 ± 1.7 Mpc [9].

The lab teaching assistant confirmed that this source had been previously observed with the Stockert Telescope, and therefore indicated that there was no need for a test observation. Therefore we proceeded to move the telescope to the respective coordinates for NGC 1073, and took an observation of 20 minutes. This observation is shown in figure 16 however, it is almost impossible to see the galaxy's detection as it is very faint in the raw data. The integration time was arbitrarily chosen from the teaching assistant's previous experience, however if the system temperature had been known beforehand, we could have also calculated the integration time from the radiometer equation (Eq. 25), where the signal to noise ratio (SNR) is of about 10 which gives an accuracy of 10%.

$$\Delta t = \mathrm{SNR}^2 \frac{1}{\Delta\nu} \left(\frac{T_{\mathrm{sys}}}{T_A} \right)^2 \tag{25}$$

Because additional noise from background and foreground sources are inevitable,

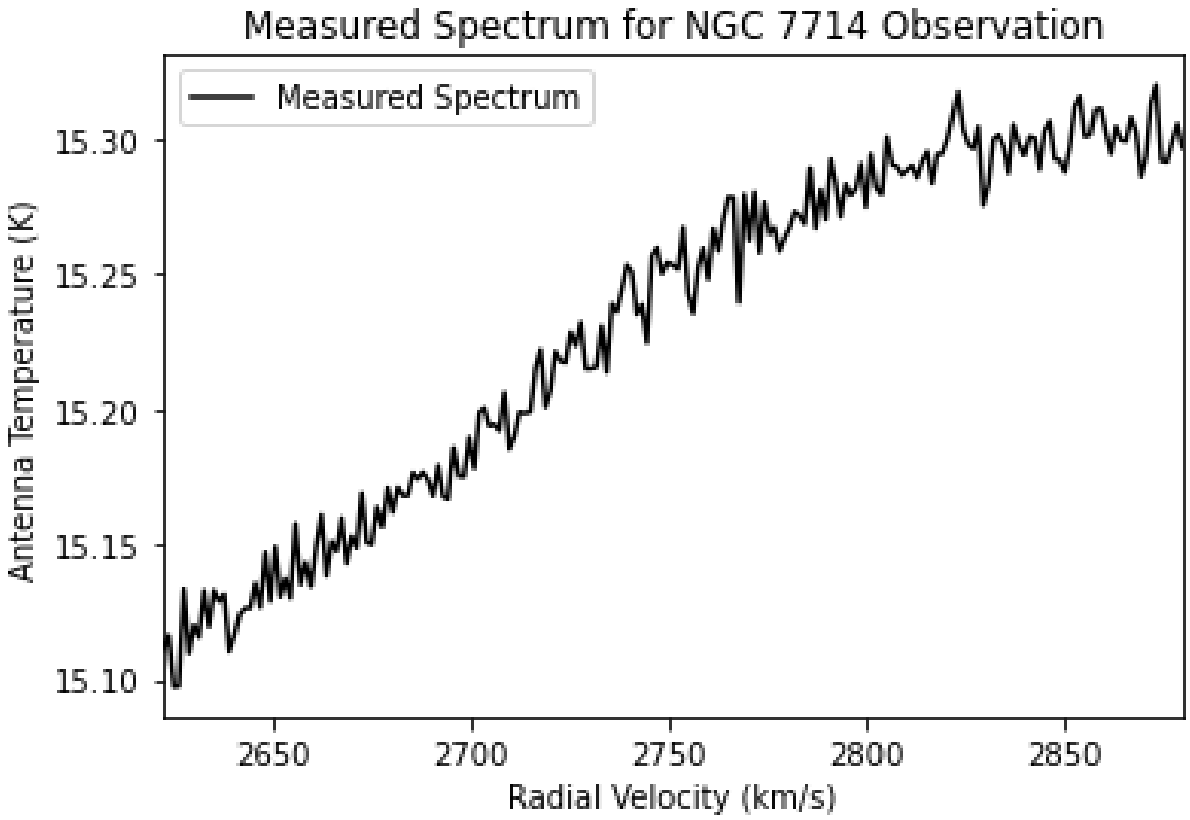

Figure 14: Measured spectrum of NGC 7714 observation which shows no detection of the galaxy.

it is also important to take an off-target observation which can be subtracted in order to reduce the noise. Although the specific right ascension and declination of the off-target observation were not provided by the telescope operator (not even present in data file, see figure 26 in the appendix), the location of the observation was chosen to be about about 1.5°off of our source galaxy, meaning that the region of observation was outside of the HPBW of 0.5°observed during the galaxy observation. This ensured that the off-target contained noise contamination from a similar region as the source observation, however, did not contain any of the same information. The observation was taken for 15 minutes and the measured spectrum of the off-target

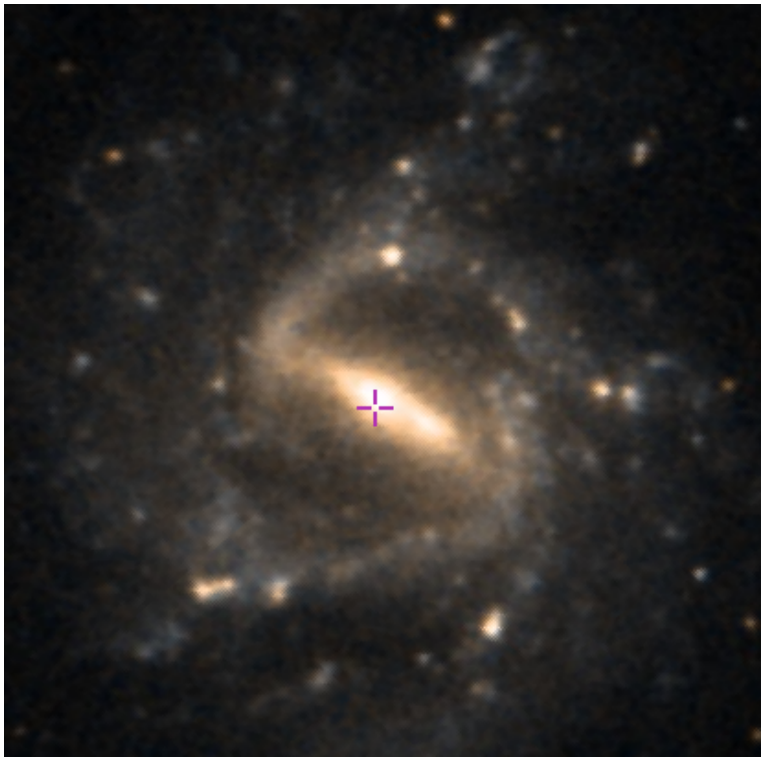

Figure 15: Image of target galaxy NGC 1073 in optical wavelengths. Source: [4]

observation is shown in figure 17 with the full off-target spectrum shown in figure 24 in the appendix.

Now that both the on-target and off-target spectrum had been measured, it was important to determine if that galaxy could be detected. The fastest way to check this was to subtract the off-target directly from the on-target as seen in Fig. 18. We make the conclusion that even though the data is extremely noisy and it is hard to make out a signal, there does indeed appear to be a double-horned peak at our expected value of radial velocity. If the observations had been of the same length we could have just used this difference for further analysis, however, this would have doubled the noise and was therefore not recommended. Instead, we were then able to fit a baseline to the off-target spectrum using the same methodology as

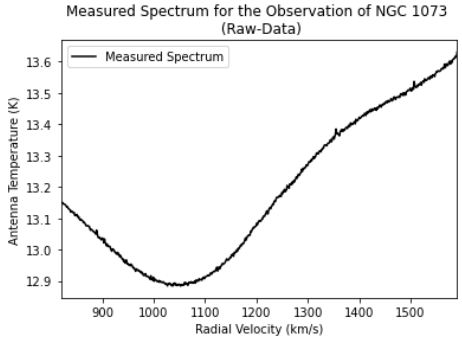

Figure 16: Measured spectrum of NGC 1074 observation. Notice how the double-horned peak is not visible.

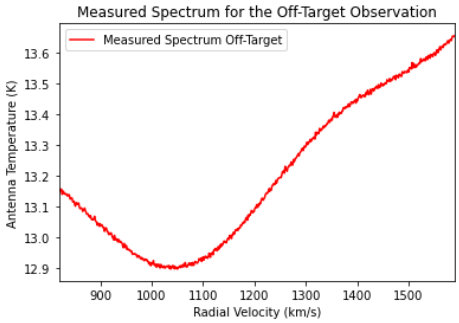

Figure 17: Measured spectrum of the off-target for the NGC 7714 observation.

in the calibration section (fitting a 5th order polynomial using the `numpy.polyfit` algorithm). The result of the fit compared to the measured spectrum is shown in figure 25 in the appendix. The baseline fit was then subtracted from the on-target observation which resulted in figure 19.

It was also important to convert the frequencies to velocities, once again using equation 19. Using the calibration factor found in the calibration section ($\alpha = 3.64 \pm 0.621$), we may now convert our measured antenna temperature T_A to the brightness temperature T_B. We can also find our uncertainty in brightness temperature using equation 22, and replacing the value for antenna temperature by brightness temperature, the same way we did in the calibration section. Using these methods find the value for the maximal brightness temperature to be:

$$T_{B,\max} = 0.0513 \pm 0.0183 \text{ K}. \tag{26}$$

The calibration factor applied to our data also gives the brightness temperature spectrum shown in figure 20.

Where it is important to remember that our data is expected to have a much lower brightness temperature than our calibration source because the signal to noise is

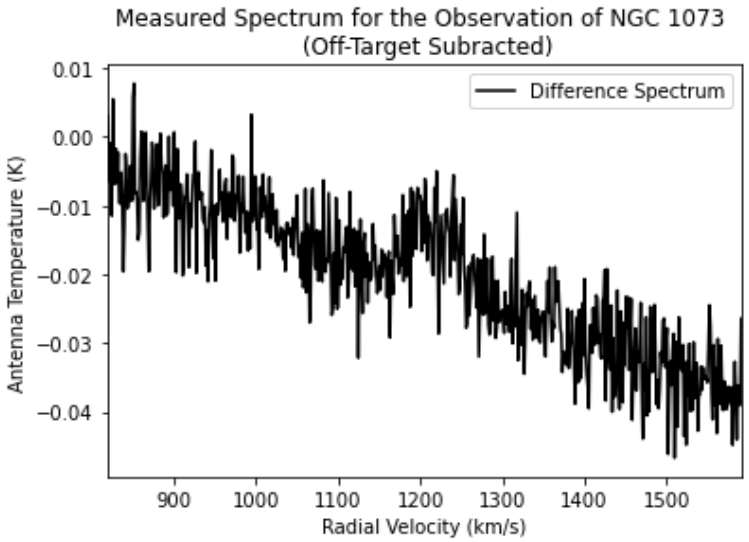

Figure 18: Measured spectrum for the observation of galaxy NGC 1073 with the off-target observation directly subtracted. Notice the small double-horned peak around a radial velocity of 1200 km/s

much lower. For the same reason, it is expected that our values for flux will be relatively low. We also calculated the systemic velocity of the profile by measuring the velocity at the center. We assuming the source is rotating, and we find that the source has profile edges at 1166 ± 10 km/s and 2560 ± 10 km/s, which gives a systemic velocity of 1863 ± 7 km/s where the uncertainty is determined from standard Gaussian error propagation (Eq.36). After this, it is important to convert the brightness temperature into a value for flux. For the Stockert telescope, we use Eq. 16, and get the result that $S_v = 0.571 \pm 0.203$ Jy, where the uncertainty can be acquired from the RMS.

We can now make the clear comparison that the galaxy profile is different than the calibration source profile in the fact that it is located at a higher velocity, and we can see the obvious double horned profile which is not present in the calibration source. The calibration source instead has 3 peaks for the 3 separate arms of the Milky Way Galaxy. One can also see that the galaxy profile has a larger width since we are

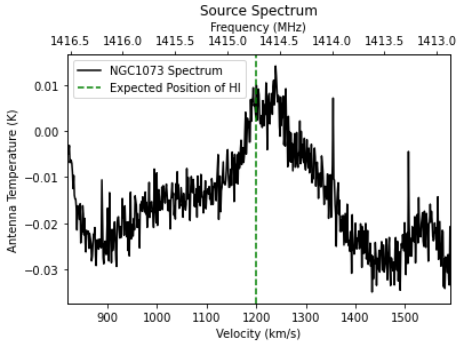

Figure 19: Measured spectrum for the observation of galaxy NGC 1073. The expected location of the HI emission is shown by the green dashed line.

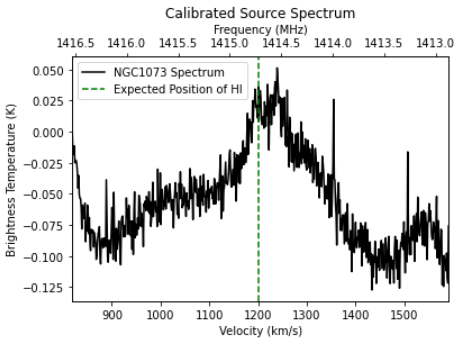

Figure 20: Calibrated spectrum for the observation of galaxy NGC 1073. The expected location of the HI emission is shown by the green dashed line.

observing more moving gas than in the calibration source. In general, it is important to note that both of these profile shapes are quite different as they represent an areas of HI gas in the Milky Way versus the entire HI gas of a separate galaxy.

The next step is to calculate the integral across the galaxy's line profile. The relevant velocity range for our source is from 1166 to 2560 km/s. Having detected a double-horn profile in our data, the best analysis would have been to use the busy function [11] to analytically describe the integrated 21-cm spectral profile. However since the python package mentioned in [11] is not well documented and has not been made available for download in a conventional manner, we use the `numpy.trapz` Python software to integrate along the non-Gaussian shape. This algorithm integrates along the given axis using the composite trapezoidal rule [16] and although it might not integrate as accurately as if we had a perfect function to describe our spectrum shape (such as in using the busy function), the integration will still be accurate enough for the purposes of this work. Using this software, we get a flux value of $S = 3.56 \pm 1.28$ Jy km/s. One might notice here that the uncertainty is relatively large, but this is expected when using Gaussian error propagation when approximating an integral (Eq. 35) and therefore applying the Gaussian equation for normally-distributed

errors (square root of the sum of squares). A better method would have been to use a more sophisticated uncertainty estimation inside the integration algorithm, however, `numpy.trapz` does not provide us with such an tool therefore simplest method is to use Gaussian error propagation (Eq. 36). Comparing this flux to the literature which finds a flux of 8.978 ± 0.050 [8], however this is most likely due to the very low signal to noise observed in our data and the fact that we are observing at somewhat lower frequencies than [8]. Taking this into account however, our results are still reasonable and therefore we can continue with the last part of galaxy data reduction.

Using this value for the integrated flux, we can then find the amount of HI mass in our source by using equation 6. Using our distance value of 12.3 ± 1.7 Mpc, and our calculated integrated flux, we find,

$$\mathrm{M_{HI}} = 1.27 \pm 0.576 \times 10^8 \mathrm{M_\odot}. \tag{27}$$

Where this uncertainty in this mass value, and the future mass values in this report are determined by standard Gaussian error propagation (Eq.36). Because this result is determined simply from the integrated flux, we would expect that the values are larger than what is found in the literature. Unfortunately, we cannot make any real comparisons due to the fact that this appears to be the first HI mass measurement of NGC 1073. According to the lab manual, in a typical galaxy, the composition of HI mass is about 10% of the baryonic mass. This means that it is possible to calculate the baryonic mass of our source to be,

$$\mathrm{M_{HI}} = 1.27 \pm 0.576 \times 10^9 \mathrm{M_\odot}. \tag{28}$$

Because most galaxies not only contain baryonic matter, but also dark matter, it is also important to include dark matter in our mass calculation. From figure 2, we can see where our galaxy (of morphological type SBc) lies in the mass to luminosity relation, and therefore assume a conversion factor of about 5 in order to convert the baryonic mass to total mass. Assuming that the total luminosity of the galaxy depends linearly on the baryonic mass, we can calculate the total mass of the galaxy

to be,

$$M_{HI} = 6.35 \pm 2.88 \times 10^{10} M_{\odot}. \quad (29)$$

Once again, here it would have been good to compare this value to the literature. The acquired mass value does however make sense if we think about the object we are observing. Since we are using a galaxy as our source, we expect our value to be similar to the typical mass value for an average galaxy ($10^{10} M_{\odot}$ [22]). Since we are conducting our analysis on an object with such a faint signal to noise, it is still rather remarkable that our values seem reasonable for a galaxy and that the entire data reduction was still successfully performed.

5.3 Data reduction of a pulsar signal

The second task of the lab was to observe a Pulsar with a known period and estimate its distance using the Dispersion Measure calculation from the Time Of Arrival (TOA) delays for the center frequencies of different frequency bands. Observing pulsars is very different from observing continuum radio emission and hence, the telescope settings were changed to the 'Pulsar Mode' which has a higher sampling rate which is required to resolve the Pulse Profile given the high rotational velocity of the stars.
paragraph

The Pulsar B0329+54 was selected for this observation. The two main motivations behind selecting this pulsar were its high flux density and comparatively low line of sight dispersion measure. B0329+54 is a pulsar in the constellation of Camelopardalis approximately at a distance of 1.695Kpc (source: ATNF Pulsar Catalogue). The pulsar is widely studied for the unusual emission components it exhibits in its emission model as well as it shows variations in these components also known as 'mode changing' in the Pulsar jargon.

The formalism of the Dispersion Measure and how it is used in calculating the dis-

tance to a pulsar is briefly discussed in section 2.2. For the scope of this experiment, the following simple parametric equations were used to calculate the DM and then determine the distance to the Pulsar:

$$\Delta t = 4.148808 \times 10ms \times (\frac{1}{{f_1}^2} - \frac{1}{{f_2}^2}) \times DM \tag{30}$$

where,
$\Delta t->$ TOA time delay between t_i and t_j
f_1, $f_2->$ Frequencies at which time delay has been recorded

$$DM = \int_0^l n_e dl \tag{31}$$

where, $l->$ Distance to the Pulsar
$n_e->$ electron density model along line of sight ($n_e = 0.028415cm^{-3}$,YMW16 Electron Density Model, [14]).
Once the Pulsar coordinates were fed into the telescope from the observatory catalogue, the telescope was slewed towards the pulsar and tracked it for roughly 10 minutes, while observing with a time resolution of 218ms. Given the high flux density of this Pulsar, the 10min observing period was enough to produce the desires Signal-to-Noise Ratio across the observing bandwidth (1430.30MHz - 1332MHz) which was split between 8 different frequency channels each covering a bandwidth of 12.3MHz respectively. Since we want to find out time delays at individual frequencies, the center frequencies of each band were identified and the TOA delay between the two extreme band center frequencies was calculated to be used in the DM and distance calculations.

The first part that was done in this analysis was getting the integrated profile of the Pulsar, integrated over all the sub-bands (Fig. 21). Note that the flux across all the frequency bands was simply added in this plot and it was not de-dispersed which will give slightly different intensity values than what should be expected from an de-dispersed pulse profile. Also note that throughout this report, arbitrary units of intensity are used, as the actual units have not been specified.

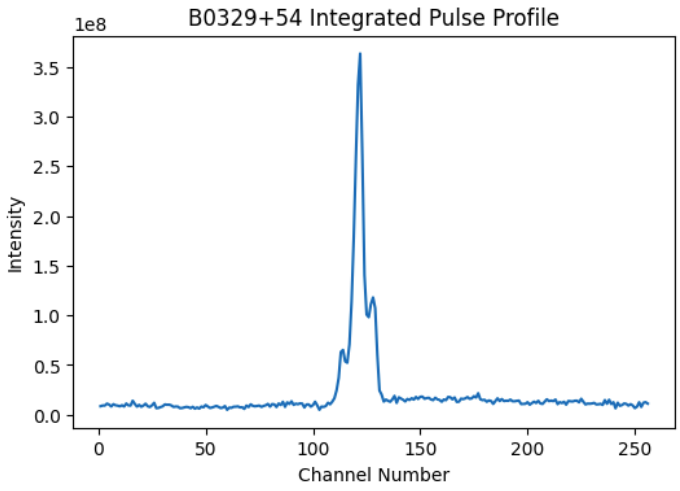

Figure 21: B0329 Pulse Profile Integrated across all (8) the frequency bands. (Notice the higher observed intensity of the profile compared to the profiles of individual bands.)

Band	Center Frequency	Channel_Number/Time_bin	Time Of Arrival(ms)
Band1	1424.24MHz	119.7 ± 4.6583	333.8433 ± 1
Band2	1411.94MHz	120.1 ± 4.6583	334.9589 ± 1
Band3	1399.64MHz	120.3 ± 4.6515	335.5167 ± 1
Band4	1387.34MHz	121 ± 4.6515	337.469 ± 1
Band5	1375.04MHz	121.4 ± 4.6515	338.5846 ± 1
Band6	1362.74MHz	121.9 ± 4.6456	339.9791 ± 1
Band7	1350.44MHz	122.2 ± 4.6456	240.8158 ± 1
Band8	1338.14MHz	122.8 ± 4.6406	342.4892 ± 1

Table 1: Time of Arrival (TOA) values calculated for each frequency band using the Peak Spectral Channel Value

The main aim of plotting the integrated profiles was to get the spectral channel number value for the peak of the profile in each sub-band which gives the Time Of

Arrival value at that specific center frequency using the simple relation given as:

$$TOA = \frac{PulsePeriod}{NumberofChannels} \times PeakChannelNumber \tag{32}$$

Refer to table 1 and figures 23, 27, 28, 29, 30, 31, 32, 33 (where the last 7 are located in the appendix) for the Gaussian fits fitted to individual profiles to get the peak spectral channel value.
The integrated profile at each spectral band was fitted with a Gaussian curve by making use of the 'astropy.modeling' [10; 15] python package wherein the fitter 'LevMarLSQFitter()' was used. The uncertainties on each Gaussian fit was calculated using the standard deviation and mean values which the fit parameters provide.

A plot between the center frequency of the band and the time of arrival is a good visual tool to understand how the interstellar medium delays the pulsar signals as a function of observing frequency (Fig. 22).

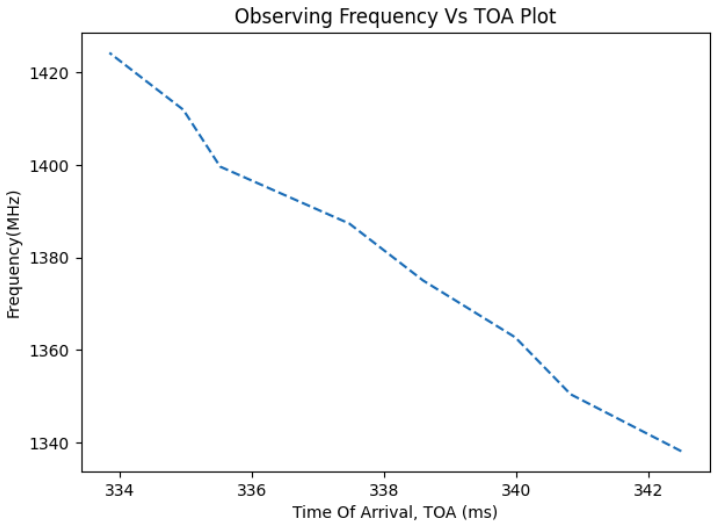

Figure 22: Dispersion delay in the received signal as it progresses towards lower frequencies

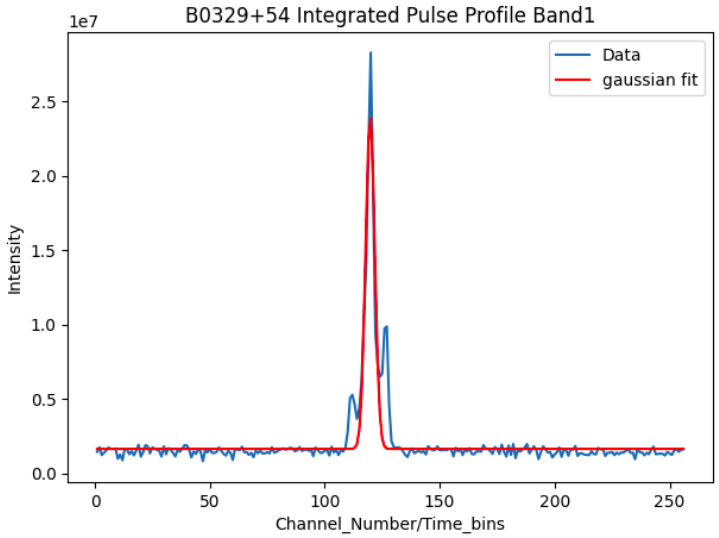

Figure 23: Band1 Pulse Profile with the Gassian Fit

To get a meaningful time delay estimate, the TOA's for the first and last frequency bands were considered while solving for DM in 30.
The Parameters:
$t_1 = 333.8433 \pm 1\text{ms}$; $t_2 = 342.4892 \pm 1\text{ms}$
$f_1 = 1424.24\text{MHz}$; $f_2 = 1338.14\text{MHz}$

Plugging in these parameters, we yield

$$DM = 31.8251 \pm 4pc\ cm^{-3} \tag{33}$$

The expected DM value from the ATNF Pulsar Catalogue is 26.7641 pc cm^{-3}. Thus, the percentage error in our measurement of the Pulsar DM was 18.9%

Using the DM value from the above equation in 31, we yield the distance to the Pulsar as,

$$l = 1.12 \pm 0.1Kpc \tag{34}$$

There is a little discrepancy in this value of the Pulsar distance. According to the old calalogued values of the pulsar distance, the expected distance is supposed to be 1.06Kpc but the current ATNF Pulsar Catalogue Value for the distance is 1.695Kpc. This is because the Australian Telescope National Facility recently updated their Pulsar Catalogue in March to a new version (V1.67) which includes details on 3319 pulsars and includes published pulsar discoveries and parameters up to December 2021, including new discoveries from PALFA and the FAST 19-beam L-Band system, a glitch table with many new entries, and numerous other small corrections.

6 Conclusion

The main goals of this report were to measure the mass of a galaxy and the distance to a pulsar. This was successfully done, with the mass of the galaxy being determined as $M_{HI} = 6.35 \pm 2.88 \times 10^{10}$ $M_{\odot}$ and the distance to the pulsar being of 1.12 ± 0.1 kpc.

There were many limitations in this project which could have been improved upon in a further project. There is always the case that observing with a larger telescope would result in a higher resolution for our data. Using a telescope such as the Effelsberg 100 m telescope for the galaxy measurement would most likely result in a more precise measurement as long as the experiment is tailored towards the specifics of this telescope. Using such a telescope would have also increased the signal to noise ratio, which would mean that it would be possible to make a more accurate measurement of the galaxy values, and therefore a more accurate mass for the galaxy. In order to get better values with the tools available, a galaxy with a higher flux could have also been chosen.

As for the dispersion measurement analysis, observing with a telescope such as the previously mentioned CHIME or LOFAR telescope would give a more precise result since observing at a lower frequency and with more bandwidth would give better results for dispersion measure observations. These specific low frequency telescopes are also larger and have more sophisticated hardware, therefore allowing for a larger number of frequency channels which in turn allows for more resolution in the frequency. This then gives a more accurate value for the time-delay, which in then helps us arrive at a more precise distance to the pulsar. This being said, one of the largest obstacles to obtaining the proper distance to a pulsar is obtaining a precise number density of electrons in the line of sight to the pulsar. This value is given from the YMW16 model and is an approximation for the part of the galaxy relevant to this experiment. Such a value could be off by up to a factor of 0.9 for 95% of pulsars in the model [14]. However, if this value were to be known with a lower uncertainty, our result for the distance to a pulsar would increase in accuracy. Overall however,

the goals for this project were all met, and the results obtained from the calculations lie within reasonable values given the circumstances of this experiment.

References

[1] Kalberla, P. M. W. / Mebold, U. / Reif, K.(1982): *Brightness temperature calibration for 21-cm line observations*, 2: 190-196.

[2] England, Martin N. / Gottesman, S. T. / Hunter, Jr.(1990): *High-Resolution Observations, Kinematics, and Dynamics of the Barred Spiral NGC 1073*456.

[3] Falco, Emilio E. u.a.(1999): *The Updated Zwicky Catalog (UZC)*, 758: 438-452.

[4] Bonnarel, F. u.a.(2000): *The ALADIN interactive sky atlas. A reference tool for identification of astronomical sources*33-40.

[5] Meyer, M. J. u.a.(2004): *The HIPASS catalogue - I. Data presentation*, 4: 1195-1209.

[6] Kaper, L. / van der Meer, A. / van Kerkwijk, M. / van den Heuvel, E.(2006): *Measuring the Masses of Neutron Stars*27-31.

[7] Skrutskie, M. F. u.a.(2006): *The Two Micron All Sky Survey (2MASS)*, 2: 1163-1183.

[8] Skrutskie, M. F. u.a.(2006): *The Two Micron All Sky Survey (2MASS)*, 2: 1163–1183.

[9] Crowther, Paul A.(2012): *On the association between core-collapse supernovae and Hii regions*, 3: 1927-1943.

[10] Astropy Collaboration u.a.(2013): *Astropy: A community Python package for astronomy*A33.

[11] Westmeier, T. / Jurek, R. / Obreschkow, D. / Koribalski, B. S. / Staveley Smith, L.(2013): *The busy function: a new analytic function for describing the integrated 21-cm spectral profile of galaxies*, 2: 1176-1190.

[12] (2014): .

[13] Guéna, J u.a.(2017): *First international comparison of fountain primary frequency standards via a long distance optical fiber link*, 3: 348–354.

[14] Yao, J. M. / Manchester, R. N. / Wang, N.(2017): *A NEW ELECTRON-DENSITY MODEL FOR ESTIMATION OF PULSAR AND FRB DISTANCES*, 1: 29.

[15] Astropy Collaboration u.a.(2018): *The Astropy Project: Building an Open-science Project and Status of the v2.0 Core Package*, 3: 123.

[16] Harris, Charles R. u.a.(2020): *Array programming with NumPy*, 7825: 357–362.

[17] Donner, J. Y. u.a.(2020): *Dispersion measure variability for 36 millisecond pulsars at 150 MHz with LOFAR*A153.

[18] Gaia Collaboration(2020): *VizieR Online Data Catalog: Gaia EDR3 (Gaia Collaboration, 2020)*I/350.

[19] Amiri, Mandana / others u.a.(2022): *An Overview of CHIME, the Canadian Hydrogen Intensity Mapping Experiment.*

[20] Astropeiler, Stockert(Not given): *Technology in numbers and videos.*

[21] Condon, James J. / Ransom, Scott M. (2016): *Essential Radio Astronomy.* .

[22] Cosmos, The SAO Encyclopedia of Astronomy (Not given): *Galaxy* `https://astronomy.swin.edu.au/cosmos/g/galaxy`, [Online; accessed 24-April-2022].

[23] Liou, Kuo Nan (1980): *An introduction to atmospheric radiation / Kuo-Nan Liou.*

.

7 Appendix

The error propagation for an addition or subtraction is given by,

$$\delta Q = \sqrt{(\delta a)^2 + (\delta b)^2 + \cdots + (\delta c)^2 + (\delta x)^2 + (\delta y)^2 + \cdots + (\delta z)^2}. \tag{35}$$

Standard Gaussian error propagation is given by the general form of Summation in Quadrature,

$$\delta f\,(x, y, ...) = \sqrt{\left(\frac{\partial f}{\partial x}\delta x\right)^2 + \left(\frac{\partial f}{\partial y}\delta y\right)^2 + \cdots} \tag{36}$$

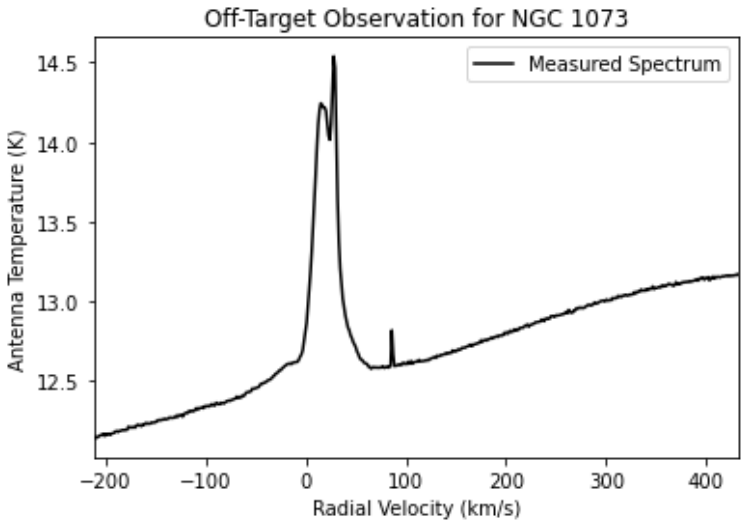

Figure 24: Measured spectrum for the off-target observation of galaxy NGC 1073.

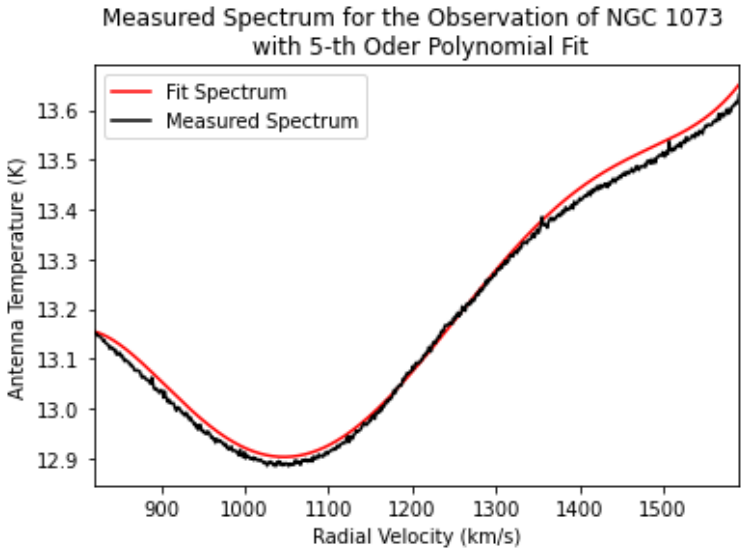

Figure 25: Measured spectrum for the observation of galaxy NGC 1073 and the off-target baseline fit.

```
SIMPLE  =                    T / conforms to FITS standard
BITPIX  =                  -32 / array data type
NAXIS   =                    1 / number of array dimensions
NAXIS1  =                16381
EXTEND  =                    T
ORIGIN  = 'STOCKERT'           / Astropeiler Stockert e.V.
TELESCOP= 'Stockert 25m'       / Telescope
T-LATITU=           50.5694444 / Latitude of telescope (WGS84)
T-LONGIT=           6.72194444 / Longitude of telescope (WGS84)
T-ALTITU=                434.0 / Altitude of telescope
SCAN-NUM=                  326 / Scan number
TIMESYS = 'UTC     '           / Time system used
DATE-OBS= '2022-04-05'         / Start date of observation
UT      = '13:16:11'           / Start time of observation
OBJECT  = 'N_A     '           / Name of target
CTYPE2  = 'RA      '           / Rectascension
CRVAL2  =                  0.0 / RA of target
CTYPE3  = 'DEC     '           / Declination
CRVAL3  =                  0.0 / DEC of target
GLAT    =                  0.0 / Galactic latitude of target
GLON    =                  0.0 / Galactic longitude of target
EPOCH   =               2000.0 / EPOCH
FRONTEN = '21 cm   '           / Front End
BACKEND = 'AFFTS   '           / Fast Fourier Spektrometer
CALFACT =           0.00068687 / Calibration factor used
CALSOUR = 'UNCALIBRATED'       / Calibration source used
CALTIME = 'NO DATE '           / Calibration date and time
LOFREQ  =         1230000000.0 / Local oscillator frequency
(nominal)           LSR-COR =                  0.0 / LSR
correction applied in km/sec              LOLSR   =
1230000000.0 / Local oscillator frequency (LSR corrected)
FSMODE  =                    F / Frequency switiching mode
DELTAF2 =                  0.0 / Offset for frequency switching
mode            LINE    = 'Hydrogen'           / Line name
BUNIT   = 'K       '           / Units are Kelvin if calibrated
RESTFREQ=         1420405752.0 / Rest frequency
OBSTIME =           890.850508 / Duration of observation
TSYS    =                   90 / Nominal system temperature
CTYPE1  = 'FREQ    '           / Type of x
CRVAL1  =                    0 / Frequency offset
CDELT1  =         -6103.515625 / Frequency resolution per
channel              CRPIX1  =                1572 / Number of
reference channel                   AZIMUTH =
0.0 / Azimuth of telescope at start of observation   ELEVATIO=
0.0 / Elevation of telescope at start of observation DAT-STOP=
'2022-04-05'         / Stop date of observation
UT-STOP = '13:31:13'           / Stop time of observation
CYCLES  =                  900 / Number of successful cycles
```

Figure 26: Parameters of off-target observation for the galaxy.

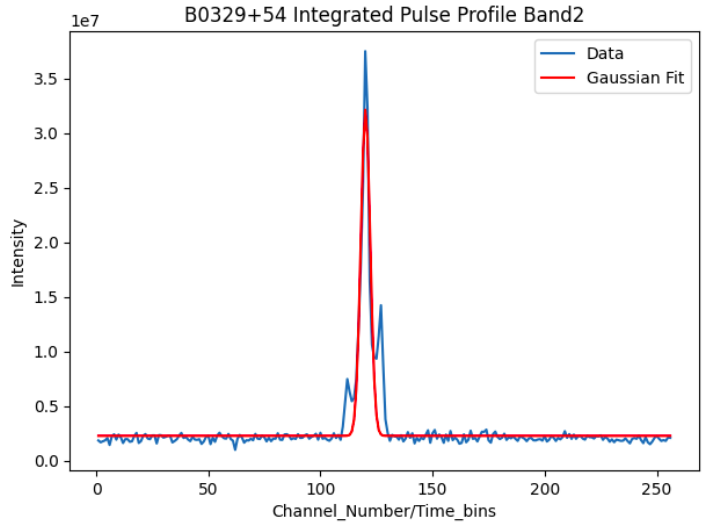

Figure 27: Band2 Pulse Profile with the Gaussian Fit

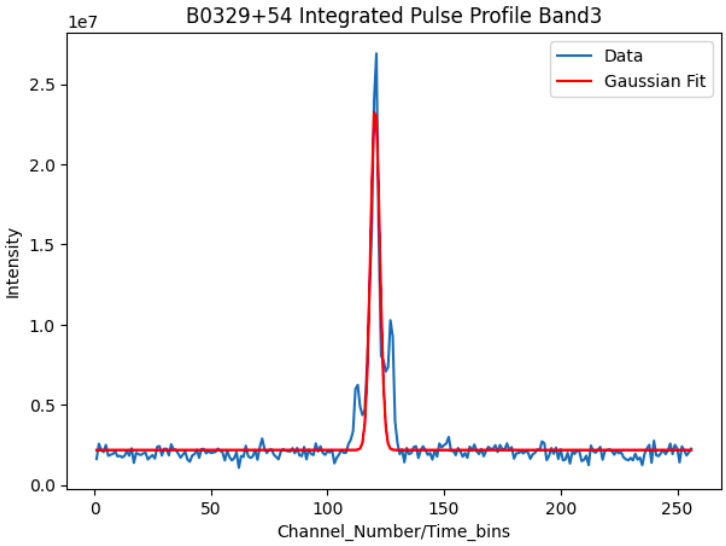

Figure 28: Band3 Pulse Profile with the Gaussian Fit

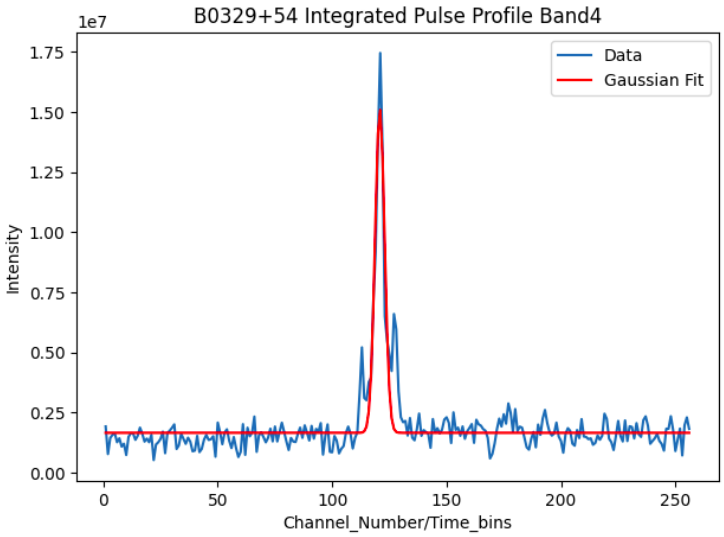

Figure 29: Band4 Pulse Profile with the Gaussian Fit

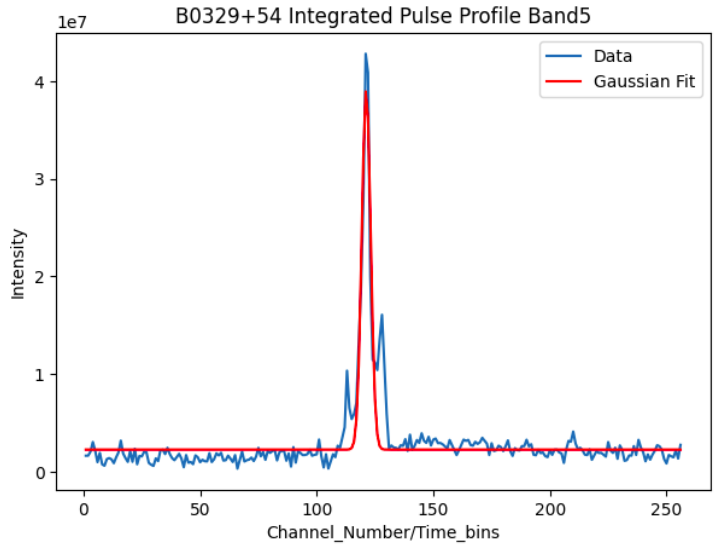

Figure 30: Band5 Pulse Profile with the Gaussian Fit

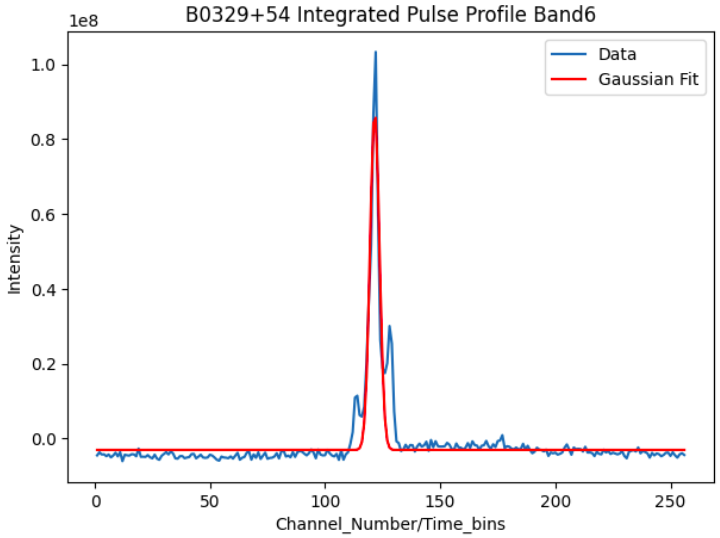

Figure 31: Band6 Pulse Profile with the Gaussian Fit

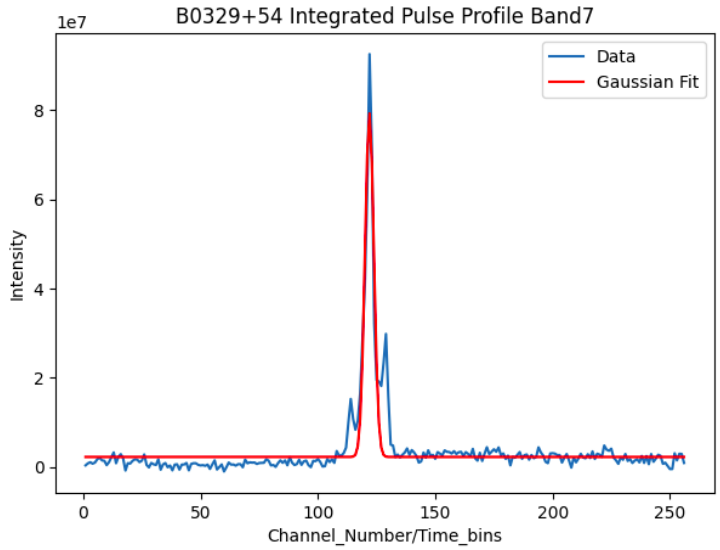

Figure 32: Band7 Pulse Profile with the Gaussian Fit

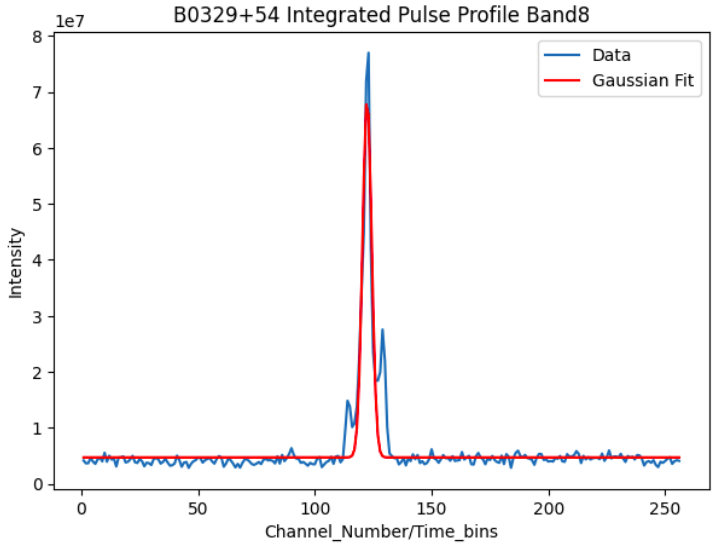

Figure 33: Band8 Pulse Profile with the Gaussian Fit